The Astrophysical Journal, 968:12 (9pp), 2024 June 10 https://doi.org/10.3847/1538-4357/ad4797

Solar Cycle Dependence of the Turbulence Cascade Rate at 1 au

Sujan Prasad Gautam[1,2], Laxman Adhikari[1,2], Gary P Zank[1,2], Ashok Silwal[1,2], and Lingling Zhao[1,2]
[1] Department of Space Science, University of Alabama in Huntsville, Huntsville, AL 35899, USA; spg0006@uah.edu
[2] Center for Space Plasma and Aeronomic Research, University of Alabama in Huntsville, Huntsville, AL 35899, USA
Received 2024 February 14; revised 2024 April 21; accepted 2024 May 3; published 2024 June 5

Abstract

We study the solar cycle dependence of various turbulence cascade rates based on the methodology developed by Adhikari et al. that utilizes Kolmogorov phenomenology. This approach is extended to derive the heating rates for an Iroshnikov–Kriachnan (IK) phenomenology. The observed turbulence cascade rates corresponding to the total turbulence energy, fluctuating magnetic energy density, fluctuating kinetic energy, and the normalized cross helicity are derived from WIND spacecraft plasma and magnetometer data from 1995 through 2020. We find that (i) the turbulence cascade rate derived from a Kolmogorov phenomenology and an IK phenomenology changes with solar cycle, such that the cascade rate is largest during solar maximum and smallest during solar minimum; (ii) the turbulence energy Kolmogorov cascade rate increases from θ_{UB} (angle between mean magnetic field and velocity) $= 0^\circ$ to 90° and peaks near $\theta_{UB} = 90^\circ$, and then decreases as θ_{UB} tends to 180°; (iii) the 2D turbulence heating rate is larger than the slab heating rate; (iv) the 2D and slab fluctuating magnetic energy density cascade rates are larger than the corresponding cascade rates of the fluctuating kinetic energy; and (v) the total turbulence energy cascade rate is positively correlated with the solar wind speed and temperature and the normalized cross-helicity cascade rate. Finally, we find that the total turbulent energy Kolmogorov cascade rate is larger than the IK cascade rate.

Unified Astronomy Thesaurus concepts: Solar wind (1534); Interplanetary turbulence (830); The Sun (1693)

1. Introduction

Turbulence is ubiquitous in the solar wind plasma (Biskamp 1996). In fully developed turbulence, the large-scale (kinetic+magnetic) turbulence energy cascades toward a smaller scale (Kolmogorov 1941) and eventually dissipates into heat energy (Matthaeus et al. 1999; Smith et al. 2001). This is one of the promising mechanisms thought to be responsible for heating the solar corona (Matthaeus et al. 1999; Oughton et al. 2001; Verdini et al. 2009; Usmanov et al. 2011; Zank et al. 2018a; Chandran & Perez 2019; Adhikari et al. 2020, 2021a; Telloni et al. 2022, 2023) and the solar wind (Smith et al. 2001, 2006; Isenberg et al. 2003; Breech et al. 2009; Ng et al. 2010; Oughton et al. 2011; Usmanov et al. 2011; Adhikari et al. 2014, 2015; Wiengarten et al. 2016; Shiota et al. 2017; Zank et al. 2018b). The turbulence cascade is driven by a variety of physical mechanisms, such as wave–particle interactions (Janser et al. 2022), magnetic reconnection (Stawarz et al. 2022), and plasma instabilities (Alexandrova et al. 2013). The turbulence cascade rate has been studied through observations (Vasquez et al. 2007; Bandyopadhyay et al. 2020), magnetohydrodynamic simulations (Chhiber et al. 2019), and remote sensing (Raja et al. 2021).

Kolmogorov (1941) proposed his famous 4/5 law, which relates the rate of dissipation of energy to the rate of energy transfer in the inertial range. According to Boldyrev (2006), the solar wind turbulence cascade rate is affected by intermittency, which refers to the presence of localized structures in the turbulence. The intermittency in the solar wind is caused by the nonlinear interaction between the magnetic and velocity fluctuations, leading to a slower cascade rate than that predicted by Kolmogorov's theory (Boldyrev 2006). However, Wu et al. (2023) found that the turbulence cascade rate in the absence of intermittency is lower than that in the presence of intermittency. The analysis of Vasquez et al. (2007) using ACE measurements suggests that the cascade rate is more consistent based on an Irosnikov–Kraichnan (IK) formulation to the Kolmogorov approach. On the other hand, Bandyopadhyay et al. (2020) used Parker Solar Probe (PSP) measurements and derived the cascade rate using a Politano–Pouquet third-order law (Politano & Pouquet 1998a) and a von Karman approach (De Karman & Howarth 1938), which follows a Kolmogorov phenomenology. Their results showed that the cascade rates obtained from both methods are approximately similar. Telloni et al. (2022) used PSP and Bepicolombo measurements at 0.11 au and 0.33 au and found turbulent magnetic energy density cascade rates of $\sim 2 \times 10^5$ J kg^{-1} s^{-1} and $\sim 1 \times 10^3$ J kg^{-1} s^{-1}, respectively. Telloni et al. (2022) also found that the cascade rate derived from the Kolmogorov phenomenology is almost similar to the cascade rate obtained from the third-order law.

At 1 au, the local heating/cascade rate varies with speed and temperature from 100 J kg^{-1} s^{-1} for the cold wind to almost 2.0×10^4 J kg^{-1} s^{-1} for the hot wind (Verma et al. 1995; Vasquez et al. 2007). For a typical slow solar wind ($U_{sw} = 400$ km s^{-1} and $T_p = 7 \times 10^4$ K) and fast solar wind ($U_{sw} = 600$ km s^{-1} and $T_p = 6 \times 10^5$ K), the heating rates are $\sim 1.0 \times 10^3$ J kg^{-1} s^{-1} and 1.3×10^4 J kg^{-1} s^{-1}, respectively (Vasquez et al. 2007). Smith et al. (2006) also found a similar heating rate of 1.1×10^3 J kg^{-1} s^{-1} at 1 au for the years 1977–1978.

According to Andrés et al. (2022), the turbulent cascade rate is different in directions parallel and perpendicular to the mean magnetic field $\mathbf{B}_0$, being larger in the perpendicular direction. MacBride et al. (2008) also analyzed ACE data sets to determine that the perpendicular turbulent cascade rate is larger than the parallel turbulent cascade rate. Adhikari et al. (2022) presented a theoretical and observational analysis of the 2D and slab cascade rates in the inner heliosphere. Their findings showed that the 2D

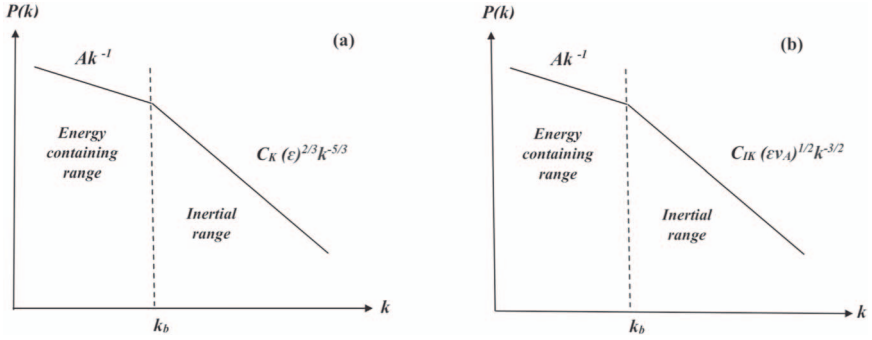

Figure 1. Schematic diagram of the power spectral density (PSD) with a Kolmogorov power law (a) and an IK power law (b) as a function of wavenumber k. k_b separates the PSD in the energy-containing range from that in the inertial range.

cascade rate dominates slab cascade rate over the inner heliospheric distance.

It is well known that the solar cycle occurs every 11 yr due to the change in the polarity of the magnetic field and changes the turbulence properties in the solar wind (Adhikari et al. 2014; Zhao et al. 2018; Zhou et al. 2020; Zhou & He 2021). This may lead to different cascade rates, e.g., Coburn et al. (2012) found different total turbulence energy cascade rates during solar maximum and solar minimum. In this particular work, we study the effect of the solar cycle on various cascade rates ϵ_{E_T}, ϵ_{E_b}, $\epsilon_{\langle u^2\rangle}$, and ϵ_{σ_c} corresponding to the total turbulence energy (E_T), fluctuating magnetic energy density (E_b), fluctuating kinetic energy $\langle u^2\rangle$, and the normalized cross helicity (σ_c), respectively, at 1 au for solar cycle 23 (SC23) and solar cycle 24 (SC24). Here, ϵ_{E_T} is the total turbulence energy cascade rate, ϵ_{E_b} is the fluctuating magnetic energy density cascade rate, $\epsilon_{\langle u^2\rangle}$ is the fluctuating kinetic energy cascade rate, and ϵ_{σ_c} is the normalized cross-helicity cascade rate. The paper is organized as follows. We discuss data selection and the method in Section 2. We present turbulence cascade theory in Section 3. Results are discussed in Section 4. Finally, the conclusion and discussion are found in Section 5.

2. Data Selection and Method

We use a 5 minutes resolution plasma and magnetometer data from WIND spacecraft over the years 1995–2020.[3] We apply the filloutliers MATLAB tool to remove large spikes in the data. First, we estimate the fluctuating magnetic energy density and fluctuating kinetic energy, outward/inward Elsässer energy $\langle z^{\pm 2}\rangle$, and the corresponding correlation lengths in a 4 hr long moving interval. To derive the fluctuating energies, we determine the variances of the fluctuations of the x, y, and z components of the magnetic field, solar wind speed, and the outward/inward Elsässer variables. To derive the correlation length, we compute the autocorrelation of the magnetic field fluctuations, velocity fluctuations, and the outward/inward Elsässer variables as a function of time lag. We then determine the time lag at which the autocorrelation function of its maximum value drops to 1/e. We convert the time lag into a distance by using Taylor's hypothesis to obtain the correlation length. In addition, we also derive the angle between the mean magnetic field and the mean solar wind speed, $\theta_{\rm UB}$.

To derive cascade rates, we adopt a method developed by Adhikari et al. (2022) based on the Kolmogorov phenomenology (hereafter, Kolmogorov cascade rate), specifically the turbulent cascade rates ϵ_{E_b}, $\epsilon_{\langle z^{\pm 2}\rangle}$, $\epsilon_{\langle u^2\rangle}$, and ϵ_{σ_c}. Based on the angle between the mean magnetic field and mean solar wind speed, we compute 2D and slab turbulence cascade rates. For this, we use two criteria: (i) $0 < \theta_{\rm UB} < 25°$ or $155° < \theta_{UB} < 180°$, and (ii) $65° < \theta_{UB} < 115°$, where criterion (i) indicates a parallel geometry between the background fields and determines the slab cascade rate and criterion (ii) indicates a perpendicular geometry between the background fields and determines the 2D cascade rate (Bieber et al. 1996; Zank et al. 2020; Adhikari et al. 2022).

Finally, we also compute the cascade rate using an Iroshnikov–Kriachnan (hereafter, IK cascade rate) for the total turbulent energy.

3. Turbulence Cascade Theory

Figure 1(a) shows a schematic diagram of the power spectral density (PSD) as a function of wavenumber k. Here, $P(k) = Ak^{-1}$ denotes the PSD in the energy-containing range, and $P(k) = C_k\epsilon^{2/3}k^{-5/3}$ denotes the PSD in the inertial range, where A is a constant to be determined, C_K is the Kolmogorov constant, and ϵ denotes the Kolmogorov cascade rate. The energy-containing range PSD is equal to the inertial range PSD at k_b, leading to (see Appendix A for the derivation; Adhikari et al. 2022)

$$\epsilon^K = \frac{E^{3/2}}{\left[C_K \log\left(\frac{1}{k_{inj}\lambda}\right)\right]^{3/2}\lambda}, \tag{1}$$

where λ is the correlation length corresponding to the turbulent energy E. We use $C_K = 1.6$ (Vasquez et al. 2007). $k_{\rm inj}$ ($\sim 1.07\times10^{-9}$ km^{-1}) is the the injection wavenumber (Adhikari et al. 2021a), which is equivalent to one solar rotation, $\sim$27 days.

Equation (1) is used to calculate the turbulent cascade rates $\epsilon^K_{E_b}$, $\epsilon^K_{\langle z^{\pm 2}\rangle}$, and $\epsilon^K_{\langle u^2\rangle}$ and are expressed as

$$\epsilon^K_{E_b} = \frac{E_b^{3/2}}{\left[C_K \log\left(\frac{1}{k_{inj}\lambda_b}\right)\right]^{3/2}\lambda_b};$$
$$\epsilon^K_{\langle z^{\pm 2}\rangle} = \frac{\langle z^{\pm 2}\rangle^{3/2}}{\left[C_K \log\left(\frac{1}{k_{inj}\lambda^{\pm}}\right)\right]^{3/2}\lambda^{\pm}};$$
$$\epsilon^K_{\langle u^2\rangle} = \frac{\langle u^2\rangle^{3/2}}{\left[C_K \log\left(\frac{1}{k_{inj}\lambda_u}\right)\right]^{3/2}\lambda_u}, \tag{2}$$

[3] https://cdaweb.gsfc.nasa.gov/

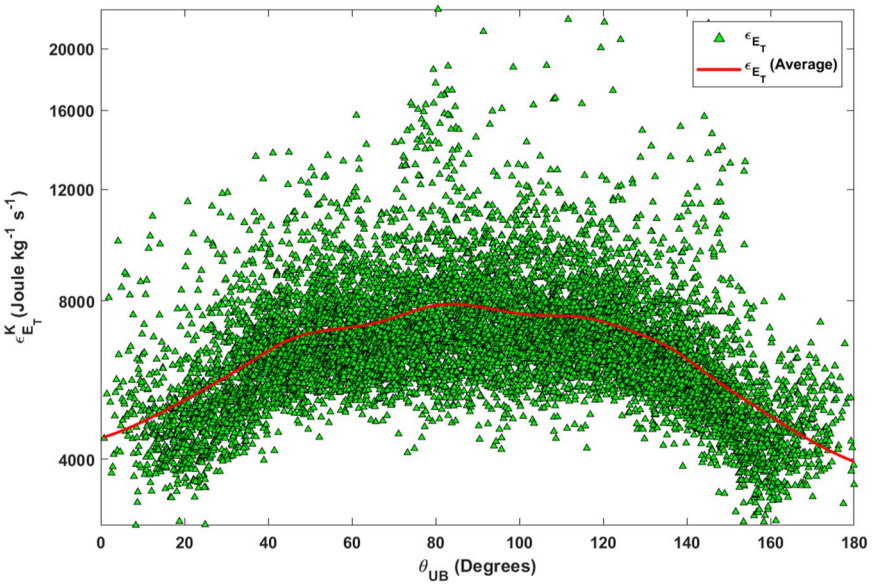

Figure 2. Total turbulent-energy cascade rate ϵ_{E_T} from 1995 to 2020 as a function of $\theta_{\rm UB}$ based on Kolmogorov phenomenology. Green triangles denote the observed turbulent-energy cascade rate, and the red curve denotes the average value.

where λ_b, $\lambda^{\pm}$, and λ_u are the correlation lengths for magnetic field fluctuations, outward and inward Elsässer energies, and the velocity fluctuations, respectively.

The schematic diagram of the PSD exhibiting the IK power law is shown in Figure 1(b). By using a procedure similar to that of Adhikari et al. (2022), the turbulent cascade rates $\epsilon^{IK}_{E_b}$, $\epsilon^{IK}_{\langle z^{\pm 2}\rangle}$, and $\epsilon^{IK}_{\langle u^2\rangle}$ become (see Appendix B for the derivation)

$$\epsilon^{IK}_{E_b} = \frac{E_b^2}{C_{IK}^2 v_A \left[\log\left(\frac{1}{k_{inj}\lambda_b}\right)\right]^2 \lambda_b};$$
$$\epsilon^{IK}_{\langle z^{\pm 2}\rangle} = \frac{\langle z^{\pm 2}\rangle^2}{C_{IK}^2 v_A \left[\log\left(\frac{1}{k_{inj}\lambda^{\pm}}\right)\right]^2 \lambda^{\pm}};$$
$$\epsilon^{IK}_{\langle u^2\rangle} = \frac{\langle u^2\rangle^2}{C_{IK}^2 v_A \left[\log\left(\frac{1}{k_{inj}\lambda_u}\right)\right]^2 \lambda_u}, \quad (3)$$

where $v_A = \frac{|B|}{\sqrt{\mu_o \rho}}$ is the Alfvén velocity. We use $C_{\rm IK} = 1.6$ (Vasquez et al. 2007). Evidently, the formulation of the turbulent cascade rate corresponding to a Kolmogorov phenomenology is different from an IK phenomenology, allowing us to distinguish between them. The turbulent cascade rates for the total turbulent energy and the normalized cross helicity are given by Breech et al. (2008), Zank et al. (2012, 2018a), and Adhikari et al. (2021b):

$$\epsilon_{E_T} = \frac{\epsilon_{\langle z^{+2}\rangle} + \epsilon_{\langle z^{-2}\rangle}}{2}; \quad \epsilon_{\sigma_c} = \frac{\epsilon_{\langle z^{+2}\rangle} - \epsilon_{\langle z^{-2}\rangle}}{\epsilon_{\langle z^{+2}\rangle} + \epsilon_{\langle z^{-2}\rangle}}. \quad (4)$$

4. Results

In this section, we present the observed turbulence cascade rates over the period of two complete SC23 and SC24.

Figure 2 shows the total turbulence energy cascade rates as a function of $\theta_{\rm UB}$ from 1995 through 2020. The green triangles represent the observed total turbulent energy cascade rates for the Kolmogorov model, and the red curve represent the average value. Clearly, $\epsilon^K_{E_T}$ varies as a function of $\theta_{\rm UB}$. Specifically, at $\theta_{\rm UB} \sim 2°$, the average $\epsilon^K_{E_T}$ is $\sim 4.2 \times 10^3$ J kg^{-1} s^{-1}. As $\theta_{\rm UB}$ increases, $\epsilon^K_{E_T}$ increases gradually until it reaches a maximum value of $\sim 7.8 \times 10^3$ J kg^{-1} s^{-1} at $\theta_{\rm UB} \sim 87°$ and then decreases as $\theta_{\rm UB}$ tends to 180°. Hence, the total turbulent energy cascade rate is higher in the vicinity of $\theta_{\rm UB} = 90°$ compared to $\theta_{\rm UB} \sim 0°$ or 180°. We note that we first derive the energy cascade rates for the outward and inward Elsässer energies. The two cascade rates are then averaged to derive the total energy cascade rate. The cascade rates for outward and inward Elsässer energies vary at their corresponding correlation lengths (e.g., Adhikari et al. 2022), but the total turbulence energy cascade rate remains the same with scale. We also note that we do not distinguish between solar maximum and solar minimum in Figure 2.

SC23 started in 1996 August, and its peak phase occurred in 2001 November, and SC24 began in 2008 December with its maximum phase in April 2014. We analyze the $\epsilon^K_{E_T}$ as a function of $\theta_{\rm UB}$ over a period of 2 yr, at different phases (minimum, moderate, and maximum) of SC23 and SC24. Figure 3 illustrates the cascade rate $\epsilon^K_{E_T}$, with the blue solid/dashed line for SC23 and the black solid/dashed line for SC24. The dashed line depicts the observed total turbulent energy cascade rate, while the solid line represents the average value. Figure 3 shows an intriguing pattern for the total turbulence energy cascade rate across different phases of solar cycles. Specifically, $\epsilon^K_{E_T}$ is smallest during the solar minimum and gradually becomes larger (moving from left to right in the upper panel of Figure 3). After reaching the solar maximum phase (bottom left panel of Figure 3), $\epsilon^K_{E_T}$ begins to decline as the solar cycles weakens (moving from left to right in the lower panel of Figure 3). We observe that the cascade rate near $\theta_{\rm UB} \sim 90°$ is larger than that near $\theta_{\rm UB} \sim 0°$ or 180° in each phase of the solar cycle. Additionally, the cascade rate during SC23 is generally larger than that during SC24. Table 1 shows the median value of $\epsilon^K_{E_T}$ and the corresponding $\theta_{\rm UB}$ during the minimum, moderate, and maximum phases of SC23 and SC24.

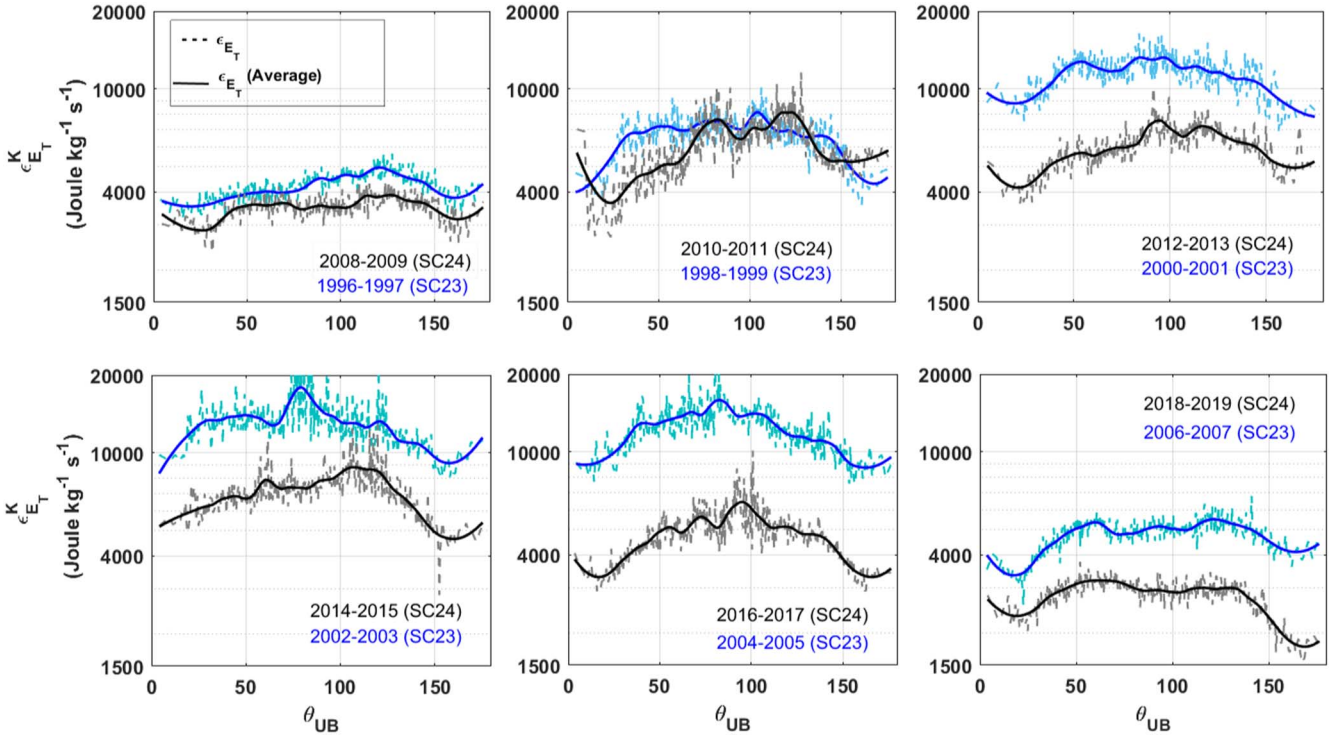

Figure 3. Total turbulent energy cascade rate for every 2 yr as a function of θ_{UB}. The blue color denotes SC23, and black represents SC24. The upper panel, from left to right, represents the ascending phase, and the lower panel, from left to right, shows the descending phase of the two solar cycles.

Table 1
The Median Value of ϵ_{E_T} and the Corresponding θ_{UB} during Different Phases of SC23 and SC24

Phases	SC23		SC24	
	ϵ_{E_T} (J kg^{-1} s^{-1})	θ_{UB} (deg)	ϵ_{E_T} (J kg^{-1} s^{-1})	θ_{UB} (deg)
Minimum	4.9×10^3	118^0	3.8×10^3	113^0
Moderate	9.0×10^3	104^0	7.8×10^3	115^0
Maximum	17.5×10^3	84^0	8.8×10^3	107^0

The properties of the solar wind plasma and turbulent heating rate become different with different solar wind temperature (T) and speed (U) conditions (Matthaeus et al. 2006; Borovsky et al. 2019). One may expect a positive correlation between the heating rate and the solar wind temperature or the heating rate and the solar wind speed. This may become different with electron temperature near the Sun (Halekas et al. 2020, 2022). However, here we only focus on the proton temperature at 1 au. In Figures 4 and 5, we plot the total turbulence energy cascade rate as a function of solar wind speed and solar wind temperature at different phases of SC23 and SC24. For each 2 yr long interval, from 2008 to 2019, we plot ϵ_{E_T} as a function of T and U for SC23 (Figure 4) and SC24 (Figure 5). In both figures, the total turbulent energy cascade rate is largest when the solar wind speed and solar wind temperature are large and vice versa. There is a very good correlation between U and T, with correlation coefficient ranging from 0.69 to 0.89, across various phases of solar cycles. This is consistent with the findings of Andrés et al. (2022). It also shows that the temperature and speed exhibit a larger correlation coefficient during solar minimum than solar active periods. In addition, Figures 4 and 5 show that during SC23, there are more yellow dots associated with large values of U and T, indicating a higher cascade rate than that in SC24. This is consistent with SC23 being stronger or more active than SC24.

We calculate the normalized cross-helicity cascade rate using Equation (4). We obtain both positive and negative values for $\epsilon^K_{\sigma_c}$. Positive $\epsilon^K_{\sigma_c}$ denotes the cascade rate dominated by the outward-propagating Alfvén waves, whereas negative $\epsilon^K_{\sigma_c}$ denotes the cascade rate dominated by the inward-propagating Alfvén waves. In this study, we find that 87% of the total $\epsilon^K_{\sigma_c}$ corresponds to a positive $\epsilon^K_{\sigma_c} > 0$ value, while 13% of the total $\epsilon^K_{\sigma_c}$ corresponds to a negative $\epsilon^K_{\sigma_c} < 0$ value. In our study, we only consider the positive $\epsilon^K_{\sigma_c} > 0$ value. In Figure 6(a), we plot the total turbulent energy cascade rate and the normalized cross-helicity cascade rate as a function of time from 1995 through 2020. Clearly, $\epsilon^K_{\sigma_c}$ varies with solar cycle, being large during solar maximum. The average value of $\epsilon^K_{\sigma_c}$ during solar maxima of SC23 and SC24 is found to be ∼0.91 and ∼0.61, respectively, while those during solar minima of SC23 and SC24 are found to be ∼0.18 and ∼0.16. Similarly, $\epsilon^K_{E_T}$ also varies as a function of time, being high during solar maximum and low during solar minimum. Equation (2) indicates that the ϵ_{E_T} is directly proportional to the turbulence energy and inversely proportional to the correlation length. Although turbulent energy varies over the solar cycle, exhibiting more

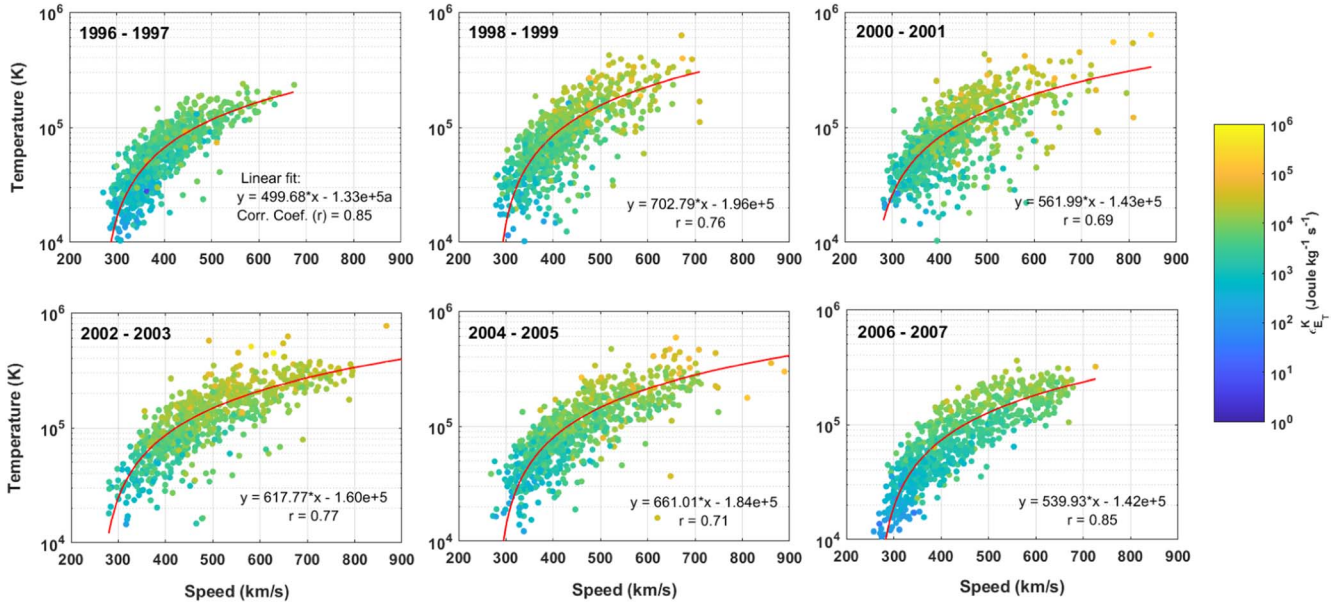

Figure 4. Total turbulent-energy cascade rate plotted as a function of solar wind speed and solar wind temperature during SC23. The format of the figure is similar to Figure 3. Red line represents a linear fit of the observed values.

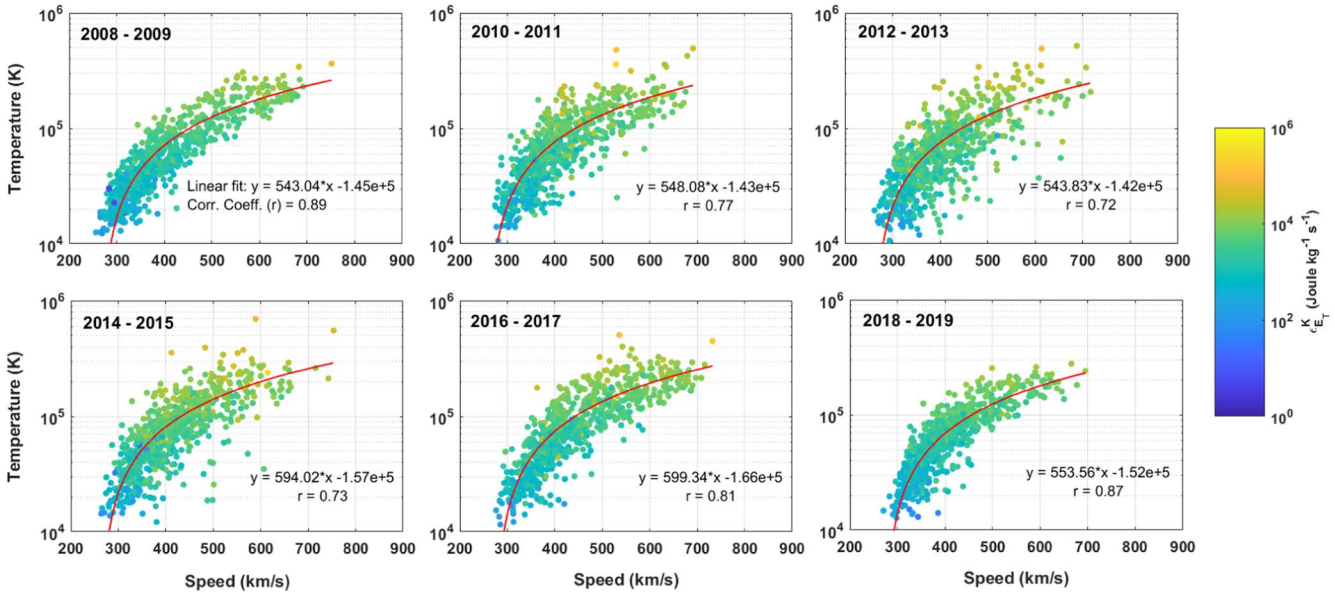

Figure 5. Total turbulent energy cascade rate plotted as a function of solar wind speed and solar wind temperature during SC24. The format of the figure is similar to Figure 3. Red lines denote a linear fit of the observed values.

turbulent energy during solar maximum (Zhao et al. 2018), we find that there is no clear dependency of the correlation length on the solar cycle. Figure 6(b) illustrates $\epsilon^K_{E_T}$ with error bars as a function of $\epsilon^K_{\sigma_c}$. In the figure, each dot corresponds to an average value over a bin width of $\epsilon^K_{\sigma_c} = 0.1$. The result shows a positive relationship between $\epsilon^K_{\sigma_c}$ and $\epsilon^K_{E_T}$, with a correlation coefficient of 0.87. At $\epsilon^K_{\sigma_c} \sim 0.9$, $\epsilon^K_{E_T}$ is found to be $\sim 1.4 \times 10^4$ J kg^{-1}, whereas at $\epsilon^K_{\sigma_c} \sim 0.05$, $\epsilon^K_{E_T}$ is found to be $\sim 0.5 \times 10^4$ J kg^{-1} s^{-1}.

Several studies (MacBride et al. 2008; Adhikari et al. 2022; Andrés et al. 2022) found that the turbulent cascade rate in a direction perpendicular to the magnetic field is larger than that in parallel direction. This difference in the heating rate in both directions is likely to related the turbulence energy being larger in the perpendicular (or 2D) direction than in the parallel (or slab) direction (Zank & Matthaeus 1992, 1993; Bieber et al. 1996; Adhikari et al. Adhikari et al Adhikari et al Adhikari et al 2022; Zank et al. 2017, 2018a, 2024). We compute the 2D and slab cascade rates by using a method described by Adhikari et al. (2022). For the slab cascade rate, we collect $\epsilon^K_{E_T}$ values corresponding to angles $\theta_{\rm UB}$ between 0^0 –25^0 or 155^0 –180^0, while for the 2D cascade rate, we consider $\epsilon^K_{E_T}$ values corresponding to angles $\theta_{\rm UB}$ between 65^0 –115^0. Figure 7(a) depicts the 2D and slab cascade rates corresponding to the total turbulence energy from 1995 to 2020. During the minimum phase of SC23, the 2D and slab cascade rates corresponding to E_T are $\sim 3.9 \times 10^3$ and $\sim 3.3 \times 10^3$ J kg^{-1} s^{-1}, respectively, and increase to $\sim 1.4 \times 10^4$ and $\sim 1.07 \times 10^4$ J kg^{-1} s^{-1}, respectively, during the maximum phase. A similar pattern

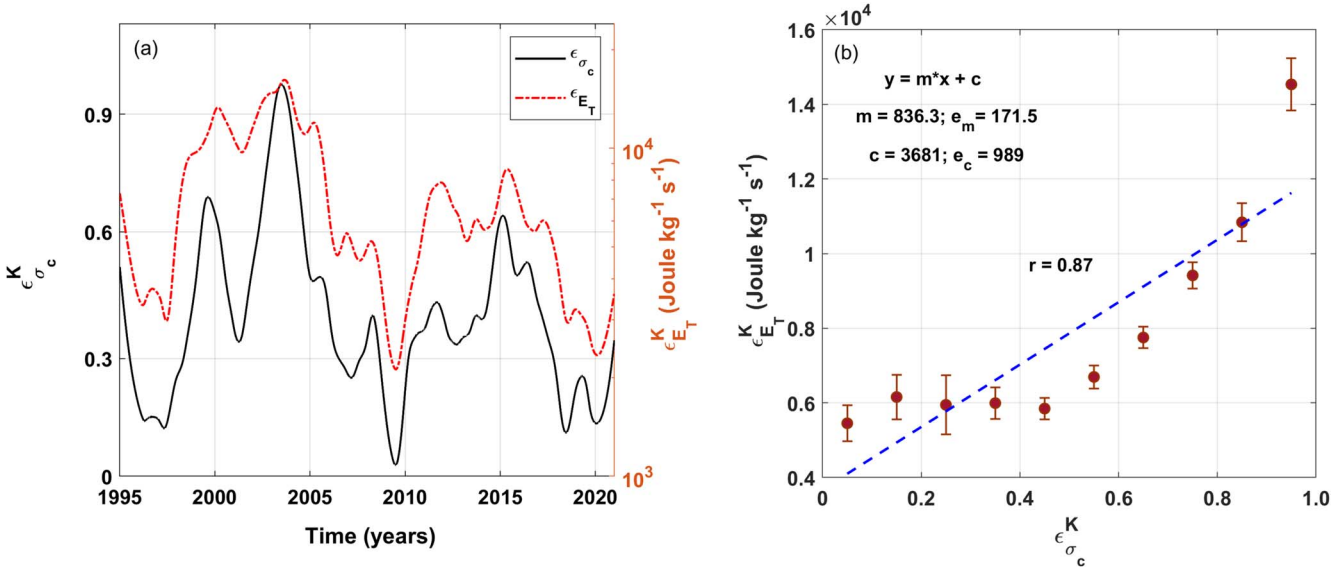

Figure 6. (a) Normalized cross-helicity cascade rate and total turbulent energy cascade rate as a function of time from 1995 through 2020. (b) Total turbulent energy cascade rate with error bars as a function of normalized cross-helicity cascade rate. $\epsilon^K_{E_T}$ is averaged over a bin width of $\epsilon^K_{\sigma_c} = 0.1$. The error bar corresponds to a standard deviation.

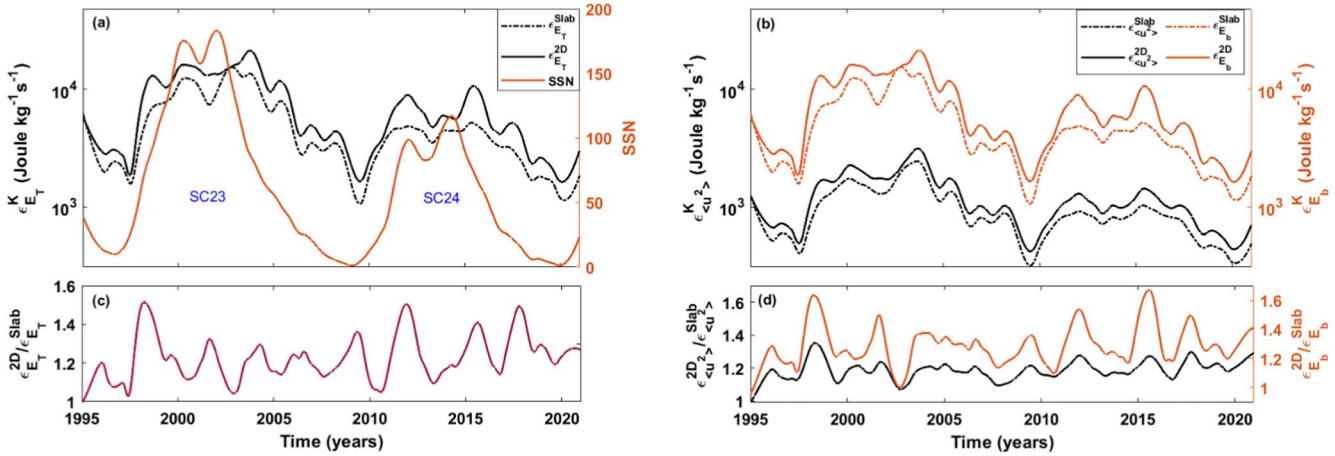

Figure 7. 2D and slab total turbulent energy cascade rates and sunspot number (a), 2D and slab cascade rates corresponding to the fluctuating kinetic and magnetic energies (c), the ratio of 2D and slab total turbulent energy cascade rate (b), and the ratio of 2D and slab fluctuating kinetic and magnetic energy cascade rates (d), as a function of time from 1995 to 2020.

emerges in SC24, with 2D and slab cascade rates corresponding to E_T being $\sim 1.4 \times 10^3$ and $\sim 1.1 \times 10^3$ J kg^{-1} s^{-1} during the solar minimum and $\sim 4.3 \times 10^3$ and $\sim 3.2 \times 10^3$ J kg^{-1} s^{-1} during the solar maximum, respectively. Figure 7(c) shows the ratio of 2D and slab total turbulent-energy cascade rates ranging between 1 and 1.6. The 2D and slab cascade rates corresponding to E_b and $\langle u^2 \rangle$ also exhibit solar cycle dependence as shown in Figure 7(b). The 2D and slab $\epsilon^K_{E_b}$ are larger than the 2D and slab $\epsilon^K_{\langle u^2 \rangle}$, respectively, for the entire solar cycle due to the fluctuating magnetic energy being larger than the fluctuating kinetic energy (Adhikari et al. 2015). Furthermore, the 2D magnetic energy density and turbulent kinetic energy cascade rates are consistently larger than the corresponding slab cascade rates throughout the solar cycle because the 2D turbulence contains more energy than slab turbulence (Zank & Matthaeus 1992; Bieber et al. 1996; Zank et al. 2017, 2020, 2024; Adhikari et al. 2017, 2021b, 2022). Figure 7(d) shows the ratio between 2D and slab cascade rates corresponding to the fluctuating kinetic energy and magnetic energy density. The 2D and slab ratio ranges between 1 and 1.7 for both $\epsilon^K_{E_b}$ and $\epsilon^K_{\langle u^2 \rangle}$. The ratio of 2D and slab turbulence cascade rates for $\epsilon^K_{E_b}$ is found to be larger than the ratio for $\epsilon^K_{<u^2>}$. The ratio of 2D and slab cascade rates during solar maximum phase to solar minimum phase is presented in Table 2. The ratio of 2D and slab cascade rates for various energies during solar maximum and solar minimum is displayed in Table 3. We note that there can be some effects of compressible fluctuations in these results as we do not calculate the heating rates particularly from the transverse (or incompressible) component. However, as the transverse component is dominant compared to the compressible component, these results may not change significantly from the results of the heating rates using the transverse components (Adhikari et al. 2022).

Vasquez et al. (2007) found that at 1 au, the IK heating rate is about an order of magnitude smaller than the Kolmogorov

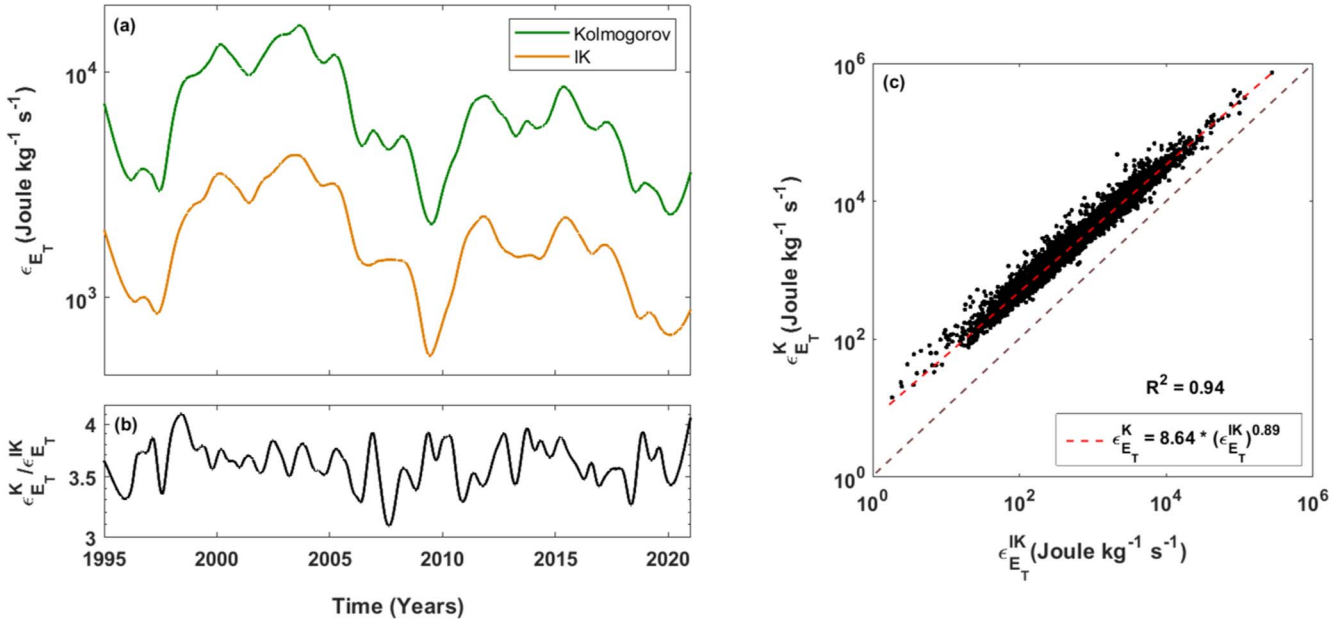

Figure 8. (a) Total turbulence energy Kolmogorov and IK cascade rates as a function of time. The green curve corresponds to the Kolmogorov cascade rate, and the yellow curve corresponds to the IK cascade rate. (b) Ratio between Kolmogorov cascade rate and IK cascade rate. (c) Kolmogorov cascade rate vs. IK cascade rate.

Table 2
Ratio of 2D and Slab Cascade Rates (ϵ^{K}) during Solar Maximum Compared to Solar Minimum for Both SC23 and SC24

Ratio	SC23	SC24
$(\epsilon^{2D}_{E_T})^{SC(\max)}/(\epsilon^{2D}_{E_T})^{SC(\min)}$	4.93	3.47
$(\epsilon^{slab}_{E_T})^{SC(max)}/(\epsilon^{slab}_{E_T})^{SC(min)}$	4.52	2.92
$(\epsilon^{2D}_{E_b})^{SC(max)}/(\epsilon^{2D}_{E_b})^{SC(min)}$	4.90	3.32
$(\epsilon^{slab}_{E_T})^{SC(max)}/(\epsilon^{slab}_{E_T})^{SC(min)}$	4.33	3.03
$(\epsilon^{2D}_{\langle u^2\rangle})^{SC(max)}/(\epsilon^{2D}_{\langle u^2\rangle})^{SC(min)}$	3.64	3.69
$(\epsilon^{slab}_{\langle u^2\rangle})^{SC(max)}/(\epsilon^{slab}_{\langle u^2\rangle})^{SC(min)}$	3.77	2.24

Table 3
Ratio between 2D and Slab Cascade Rates (ϵ^{K}) during Solar Maximum and Solar Minimum

Ratio	$SC23^{min}$	$SC23^{max}$	$SC24^{min}$	$SC24^{max}$
$\epsilon^{2D}_{E_T}/\epsilon^{slab}_{E_T}$	1.14	1.32	1.13	1.31
$\epsilon^{2D}_{E_b}/\epsilon^{slab}_{E_b}$	1.17	1.32	1.23	1.28
$\epsilon^{2D}_{\langle u^2\rangle}/\epsilon^{slab}_{\langle u^2\rangle}$	1.13	1.21	1.09	1.17

cascade rate. We also derive the total turbulence IK heating rate ($\epsilon^{IK}_{E_T}$) and compare it with the Kolmogorov cascade rate ($\epsilon^{K}_{E_T}$) as shown in Figure 8(a). Both the Kolmogorov and IK heating rates exhibit similar trends as a function of time from 1995 to 2020 although the former is larger than the latter heating rate from 1995 through 2020. Figure 8(b) shows the ratio between the Kolmogorov heating rate and the IK heating rate, which ranges between 3.1 and 4.1, with a mean value of 3.5. In Figure 8(c), we plot the Kolmogorov heating rate vs. the IK heating rate. The correlation coefficient between $\epsilon^{K}_{E_T}$ and $\epsilon^{IK}_{E_T}$ is found to be 0.97, indicating that the Kolmogorov and IK heating rates are highly correlated. The Kolmogorov and IK heating rates show a relationship of $\epsilon^{K}_{E_T} \sim (\epsilon^{IK}_{E_T})^{0.89}$, i.e., a nearly linear relationship.

5. Discussion and Conclusions

We studied the solar cycle dependence of various turbulent cascade rates, along with the 2D and slab cascade rates, using the magnetometer and plasma data from the WIND spacecraft from 1995 through 2020. We derived the observed turbulent cascade rates corresponding to the total turbulent energy, fluctuating magnetic energy density, fluctuating kinetic energy, and the normalized cross helicity using a Kolmogorov phenomenology. Similarly, we derived the total turbulence-energy cascade rate using an IK phenomenology. For the Kolmogorov approach, we used the equation for the heating rate from Adhikari et al. (2022). For the IK phenomenology, we derived an equation for the heating rate using an approach similar to that of Adhikari et al. (2022). We summarize our findings as follows.

1. The total turbulence energy cascade rate, derived from both a Kolmogorov phenomenology and an IK phenomenology, changes with solar cycle, being largest during solar maximum and lowest during solar minimum. The total turbulence energy heating rate during SC23 is larger than that of SC24, indicating a larger heating rate during a stronger solar cycle.
2. The total turbulence energy cascade rate increases from $\theta_{UB} = 0^0$ to 90^0, peaks near 90^0, and then decreases as θ_{UB} tends to 180^0 for each phase (minimum, moderate, and maximum; see Table 1) of SC23 and SC24.
3. The 2D and slab cascade rates corresponding to the total turbulence energy, magnetic energy density, and the fluctuating kinetic energy vary with solar cycle, being larger during solar maximum than during solar minimum (Table 2).
4. The 2D turbulence cascade rate corresponding to the total turbulence energy, fluctuating magnetic energy, and the fluctuating kinetic energy is larger than the corresponding slab cascade rates from 1995 to 2020. The larger 2D

cascade rate than the slab cascade rate (Table 3) is consistent with the results of MacBride et al. (2008), Adhikari et al. (2022), Andrés et al. (2022). This indicates that 2D turbulence is primarily responsible for heating the solar wind (Zank & Matthaeus 1992, 1993; Adhikari et al. 2017, 2018a, 2020; Telloni et al. 2022, 2023).

5. The 2D and slab fluctuating magnetic energy cascade rates are larger than the corresponding 2D and slab cascade rates for the fluctuating kinetic energy from 1995 through 2020. This is consistent with the results of Adhikari et al. (2022).
6. The total turbulent energy Kolmogorov cascade rate is found to be larger than the total turbulent energy IK cascade rate, in accord with the findings of Vasquez et al. (2007).
7. The total turbulence energy cascade rate is positively correlated with the solar wind speed, temperature, and the normalized cross-helicity cascade rate.

This study provides evidence that the turbulence heating rate depends on solar cycle. We derived various cascade rates, along with the 2D and slab cascade rates, using a Kolmogorov and an IK phenomenology. We found that the turbulence cascade rate is higher during the solar maximum than solar minimum. These results differ from those of Coburn et al. (2012). In this work, the turbulent cascade rate is directly proportional to the turbulence energy and inversely proportional to the correlation length. During solar maximum, the turbulence energy is larger than that during the solar minimum (e.g., Zhao et al. 2018), resulting in a larger cascade rate in the prior case than the latter case. In addition, Stawarz et al. (2009) suggests that the inclusion of shocks and their driver gases can increase the cascade rates. We note that the expression for the turbulence cascade rate (Adhikari et al. 2021b) was derived based on the Kolmogorov (or IK) phenomenology, which avoids the shock transient events. In the observational analysis, we also excluded all shock events. We also note that the correlation length was not found to depend on the solar cycle. This result may change in the case of solar cycle dependence on the correlation length. The observed cascade rates can be compared with the results derived from other methods such as third-order law (Politano & Pouquet 1998a, 1998b) and 2D +slab model (MacBride et al. 2008).

Acknowledgments

We acknowledge the partial support of a Parker Solar Probe contract SV4-84017, an NSF EPSCoR RII-Track-1 cooperative agreement OIA-2148653, NASA award 80NSSC21K1319, NASA Heliospheric Shield 80NSSC22M0164, and the SWAP instrument effort on the New Horizons project (M99023MJM; PU-A WD1006357), with support from NASA's New Frontiers Program and the IMAP mission as a part of NASA's Solar Terrestrial Probes (STP) mission line (80GSFC19C0027). A.S. and L.L.Z. acknowledge the partial support of the NASA awards 80NSSC20K1783 and 80NSSC23K0415. We acknowledge CDAWeb (https://cdaweb.gsfc.nasa.gov/) for providing the plasma and magnetometer data set.

Appendix A
Cascade Rate: Kolmogorov Phenomenology

The energy-containing range PSD, i.e., $P(k) = Ak^{-1}$, is equal to the inertial range PSD, i.e., $P(k) = C_k\epsilon^{2/3}k^{-5/3}$, at k_b, where k_b separates the energy-containing range and inertial range (Figure 1(a)). Here, A is a constant to be determined. Therefore, we write

$$Ak^{-1}|_{k_b} = C_K\,\epsilon^{2/3}k^{-5/3}|_{k_b}; \tag{A1}$$

$$\Rightarrow \epsilon^K = \left[\frac{A}{C_K}k_b^{2/3}\right]^{3/2}. \tag{A2}$$

Integration of $P(k) = Ak^{-1}$ from the injection wavenumber ($k_{\rm inj}$) to k_b yields

$$E = \int_{k_{inj}}^{k_b} Ak^{-1}; \tag{A3}$$

$$\Rightarrow A = \frac{E}{\log\left(\frac{k_b}{k_{inj}}\right)}. \tag{A4}$$

Here, the denominator is dimensionless, and the numerator has a dimension of energy. So, A has a dimension of energy. Therefore, from Equations (A2) and (A4), the equation for the turbulence cascade rate can be derived in the form

$$\epsilon^K = \left[\frac{E}{C_K}\frac{k_b^{2/3}}{\log\left(\frac{k_b}{k_{inj}}\right)}\right]^{3/2}; \tag{A5}$$

$$\Rightarrow \epsilon^K = \frac{E^{3/2}}{\left[C_K\log\left(\frac{1}{k_{inj}\lambda}\right)\right]^{3/2}\lambda}, \tag{A6}$$

where we assume that $k_b = \lambda^{-1}$ (λ is the correlation length corresponding to the turbulent energy E).

Appendix B
Cascade Rate: IK Phenomenology

Equating the PSD of energy-containing range and the inertial range (Figure 1(b)) gives

$$Ak^{-1}|_{k_b} = C_{IK}(\epsilon v_A)^{1/2}k^{-3/2}|_{k_b}; \tag{B1}$$

$$\Rightarrow \epsilon^{IK} = \frac{A^2}{C_{IK}^2 v_A}\frac{1}{\lambda}. \tag{B2}$$

Using Equation (A4), Equation (B2) reduces to

$$\epsilon^{IK} = \frac{E^2}{C_{IK}^2 v_A\left[\log\left(\frac{1}{k_{inj}\lambda}\right)\right]^2\lambda}. \tag{B3}$$

ORCID iDs

Sujan Prasad Gautam https://orcid.org/0000-0001-7379-4268
Laxman Adhikari https://orcid.org/0000-0003-1549-5256
Gary P Zank https://orcid.org/0000-0002-4642-6192
Ashok Silwal https://orcid.org/0000-0001-6286-2106
Lingling Zhao https://orcid.org/0000-0002-4299-0490

References

Adhikari, L., Zank, G., Hunana, P., et al. 2017, ApJ, 841, 85
Adhikari, L., Zank, G., Zhao, L.-L., & Telloni, D. 2022, ApJ, 938, 120

Adhikari, L., Zank, G., Zhao, L.-L., et al. 2021b, A&A, 656, A6
Adhikari, L., Zank, G. P., Bruno, R., et al. 2015, ApJ, 805, 63
Adhikari, L., Zank, G. P., & Zhao, L. 2021a, Fluids, 6, 368
Adhikari, L., Zank, G. P., & Zhao, L.-L. 2020, ApJ, 901, 102
Alexandrova, O., Chen, C. H. K., Sorriso-Valvo, L., Horbury, T. S., & Bale, S. D. 2013, SSRv, 178, 101
Andrés, N., Sahraoui, F., Huang, S., Hadid, L., & Galtier, S. 2022, A&A, 661, A116
Bandyopadhyay, R., Goldstein, M., Maruca, B., et al. 2020, ApJS, 246, 48
Bieber, J. W., Wanner, W., & Matthaeus, W. H. 1996, JGRA, 101, 2511
Biskamp, D. 1996, Ap&SS, 242, 165
Boldyrev, S. 2006, PhRvL, 96, 115002
Borovsky, J. E., Denton, M. H., & Smith, C. W. 2019, JGRA, 124, 2406
Breech, B., Matthaeus, W. H., Cranmer, S., Kasper, J., & Oughton, S. 2009, JGRA, 114, A09103
Breech, B., Matthaeus, W. H., Minnie, J., et al. 2008, JGRA, 113, A08105
Chandran, B. D., & Perez, J. C. 2019, JPlPh, 85, 905850409
Chhiber, R., Usmanov, A. V., Matthaeus, W. H., Parashar, T. N., & Goldstein, M. L. 2019, ApJS, 242, 12
Coburn, J. T., Smith, C. W., Vasquez, B. J., Stawarz, J. E., & Forman, M. A. 2012, ApJ, 754, 93
De Karman, T., & Howarth, L. 1938, RSPSA, 164, 192
Halekas, J., Whittlesey, P., Larson, D., et al. 2020, ApJS, 246, 22
Halekas, J., Whittlesey, P., Larson, D., et al. 2022, ApJ, 936, 53
Isenberg, P. A., Smith, C. W., & Matthaeus, W. H. 2003, ApJ, 592, 564
Janser, S., Saur, J., Clark, G., Sulaiman, A., & Szalay, J. 2022, JGRA, 127, e2022JA030675
Kolmogorov, A. N. 1941, DoSSR, 30, 301
Adhikari, L., Zank, G., Hu, Q., & Dosch, A. 2014, ApJ, 793, 52
MacBride, B. T., Smith, C. W., & Forman, M. A. 2008, ApJ, 679, 1644
Matthaeus, W., Elliott, H., & McComas, D. 2006, JGRA, 111, A10103
Matthaeus, W. H., Zank, G. P., Smith, C. W., & Oughton, S. 1999, PhRvL, 82, 3444
Ng, C., Bhattacharjee, A., Munsi, D., Isenberg, P., & Smith, C. 2010, JGRA, 115, A02101
Oughton, S., Matthaeus, W. H., Dmitruk, P., et al. 2001, ApJ, 551, 565
Oughton, S., Matthaeus, W. H., Smith, C. W., Breech, B., & Isenberg, P. 2011, JGRA, 116, A08105
Politano, H., & Pouquet, A. 1998a, GeoRL, 25, 273
Politano, H., & Pouquet, A. 1998b, PhRvE, 57, R21
Raja, K. S., Subramanian, P., Ingale, M., Ramesh, R., & Maksimovic, M. 2021, ApJ, 914, 137
Shiota, D., Zank, G., Adhikari, L., et al. 2017, ApJ, 837, 75
Smith, C. W., Isenberg, P. A., Matthaeus, W. H., & Richardson, J. D. 2006, ApJ, 638, 508
Smith, C. W., Matthaeus, W. H., Zank, G. P., et al. 2001, JGRA, 106, 8253
Stawarz, J., Eastwood, J., Phan, T., et al. 2022, PhPl, 29, 012302
Stawarz, J. E., Smith, C. W., Vasquez, B. J., Forman, M. A., & MacBride, B. T. 2009, ApJ, 697, 1119
Telloni, D., Adhikari, L., Zank, G. P., et al. 2022, ApJL, 938, L8
Telloni, D., Romoli, M., Velli, M., et al. 2023, ApJL, 955, L4
Usmanov, A. V., Matthaeus, W. H., Breech, B. A., & Goldstein, M. L. 2011, ApJ, 727, 84
Vasquez, B. J., Smith, C. W., Hamilton, K., MacBride, B. T., & Leamon, R. J. 2007, JGRA, 112, A07101
Verdini, A., Velli, M., Matthaeus, W. H., Oughton, S., & Dmitruk, P. 2009, ApJL, 708, L116
Verma, M., Roberts, D., & Goldstein, M. 1995, JGRA, 100, 19839
Wiengarten, T., Oughton, S., Engelbrecht, N., et al. 2016, ApJ, 833, 17
Wu, H., Huang, S., Wang, X., Yang, L., & Yuan, Z. 2023, ApJL, 958, L28
Zank, G., Adhikari, L., Hunana, P., et al. 2017, ApJ, 835, 147
Zank, G., Adhikari, L., Hunana, P., et al. 2018a, ApJ, 854, 32
Zank, G., Dosch, A., Hunana, P., et al. 2012, ApJ, 745, 35
Zank, G., & Matthaeus, W. 1992, JPlPh, 48, 85
Zank, G., Nakanotani, M., Zhao, L.-L., Adhikari, L., & Telloni, D. 2020, ApJ, 900, 115
Zank, G. P., Adhikari, L., Zhao, L.-L., et al. 2018b, ApJ, 869, 23
Zank, G. P., & Matthaeus, W. 1993, PhFlA, 5, 257
Zank, G. P., Zhao, L.-L., Adhikari, L., et al. 2024, ApJ, 966, 75
Zhao, L.-L., Adhikari, L., Zank, G., Hu, Q., & Feng, X. 2018, ApJ, 856, 94
Zhou, G., & He, H.-Q. 2021, ApJL, 911, L2
Zhou, G., He, H.-Q., & Wan, W. 2020, ApJL, 899, L32